The Cloud Structure of the Jovian North Equatorial Zone: Context of the Galileo Probe Entry Latitude

Sarah T. Stewart*
Division of Geological and Planetary Sciences
California Institute of Technology
Pasadena, CA 91125

Glenn S. Orton*, Brendan M. Fisher*,†, Kevin H. Baines*
Earth and Space Sciences Division
Jet Propulsion Laboratory
California Institute of Technology
Pasadena, CA 91109

11 September 1997

Short title: *Equatorial Cloud Structure*
Submitted to: Journal *of Geophysical Research-Planets*
Figures: 8
Tables: 4

Send correspondence to:
Sarah T. Stewart
Caltech M.S. 150-21
Pasadena, CA 91125
sstewart@caltech.edu

* Visiting astronomer at the Infrared Telescope Facility, which is operated by the University of Hawaii under contract from the National Aeronautics and Space Administration.
† NASA/NRC Resident Research Associate.

Abstract

We present a dataset of grouud-based full-disk images of Jupiter from 1.58 to 5.30 μm with the utility of an imaging spectrometer with 1°x1° resolut ion. The spectral coverage is sensitive to the vertical cloud structure from ~10 mbar to $\gtrsim$ 5 bar. Tile northern Equatorial Zone and southern North Equatorial Belt have been examined in detail to provide ground-truth context for the Galileo probe data. A modified version of the single-scat tering cloud inversion technique developed by Banfield *et al.* (1996) has been applied to the data to create three-dimensional maps of the vertical cloud structure throughout this region. We make no assumptions about the initial vertical cloud structure iu this retrieval.

We detect three distinct cloud layers iu the upper atmosphere: a thiu stratospheric haze located $\gtrsim$ 20 mbar; a relatively homogeneous upper tropospheric cloud based bet ween ~350-460 mbar; aud a highly variable lower tropospheric cloud layer whose top has been detected between 1.5 aud 3.0 bar in various locations. The optical depths of t hew clouds are $\lesssim$ 0.01, ~0.5, aud $\gtrsim$ 2.0, respectively, at 2 μm.

The upper tropospheric layer changes slightly over 5-μm hot spots relative to their surrounding regions. The elevation of the cloud base increases slightly over hot spots (ΔP ~20 mbar), and there is a decrease in opacity of ~10% at 2μm. If the upper tropospheric CLOUCL is the main ammonia cloud at the condensation level, the ammonia mixing ratio is only a few percent of solar in the upper atmosphere ($P < 1$ bar) throughout the equatorial region.

1 Introduction

The Jovian cloud structure is intimately related to the composition of the atmosphere and is the primary tracer for the dynamics of the upper atmosphere. The study of these clouds is, therefore, one course in the pursuit of these fundamental questions about Jupiter. The canonical Jovian three-cloud structure was based on chemical equilibrium theory of cloud condensation levels with mar-solar abundances of the major atmospheric constituents (Weidenschilling aud Lewis 1973). Much of the subsequent study of Jovian clouds has used some of the predictions of this theory as *a priori* values (see Ragent *et al. 1997,* for an summary of cloud studies to date and West *et al. 1986,* for an extensive synthesis of Jovian cloud data to that date).

On December 7, 1995, the Galileo probe conducted the first *in situ* measurements of the Jovian atmosphere, entering a region of the planet known as a 5-μm hot spot (Orton *et* al. 1996), a region defined by decreased cloud opacity resulting in increased thermal radiance from deep within the planet aud reduced reflectivity in the visible. The data from the probe proved surprising: strong depletion in volatiles relative to solar abundances (Neimann *et al.* 1996) and a single, tenuous cloud at 1.34 bar (Ragent *et al.* 1997). These results have led to a renewed effort to characterize the cloud structure of 5-μm hot spots aud its relationship to the rest of the planet. Ground-based data are well suited for this study, where there is extensive coverage of the planet in time, and a necessary supplement to the Galileo mission with its reduced data rate. We present an analysis of the data with as few initial assumptions as possible, to minimize the questions of uniqueness.

We present our dataset in section 2. In section 3, we explain the single scattering inversion analysis. We interpret the retrieved cloud profiles and examine the question of uniqueness in section 4. The direct results from this analysis is presented in section 5. The opacities of the cloud levels are calculated using multiple scattering in section 6. We discuss the implications of our results in section 7.

2 The Dataset

The data in this study consist of images collected at the NASA Infrared Telescope Facility (IRTF), on Mauna Kea, Hawaii, on May 20, 1995, aud April 25, 1996, using the facility near-infrared camera, NSFCAM, with its $\sim$1.5% circular variable filter (CVF) from 1 .58 to 5.30 μm. Table I presents our data coverage. The full disk images were exposed in quick succession, building a dataset in the manner of au imaging spectrometer. The plate scale is 0.3015 arcseconds per pixel, resulting in a maximum Jovian resolution of just under one degree per pixel. The data reduction process was standard: sky subtraction, flat fielding, interpolation over bad pixels (5σ rejection threshold), and calibration, followed by cylindrical map projection in System 111 longitude ant] planetocentric latitude.

The images taken on May 20, 1995, were photometrically calibrated against α Libra ($\lambda < 4.0\mu$m) and α Boo ($\lambda > 4\mu$m) at exactly the same airmass (1.3). The seeing was trotter than one arcsecond. The April 25, 1996, images were calibrat ed by a least squares fit of t he central meridian to the May 20, 1995 dataset and a set of NSFCAM CVF images from June 28, 1996, which was photometrically calibrated against ν_2 Sagittarii (BS 7120). Finally, the mar-infrared (NIR) wavelengths ($\lambda < 4.0\mu$m) were converted to reflectivity units, I/F. The error bars vary with wavelength from 5 to 40% (refer to Fig. 1); α Libra and α Boo's absolute fluxes were assumed to have an error of 5%. The wavelengths with larger error bars (2.27, 3.80, 3.986, 4.55, 5.30 μm)

are primarily due to observational noise. For the purposes of this analysis, the maps have been linearly interpolated to a resolution of 1°x1° per pixel. For comparison, the Galileo Near Infrared Mapping Spectrometer (NIMS) has a typical spatial resolution of about 0.3°x0.30, and the Solid State imaging (SS1) system has an average spatial resolution of about 0.03°x0.030. As the data were obtained in a short time interval (< 20 minutes), the maps were not shifted to account for zonal winds because their effects are less than our binned resolution.

The wavelengths have been chosen to cover the H (from 1.58-1.85 μm), K (from 2.0-2.27 μm) and 5 μm atmospheric windows. In the Jovian atmosphere, these NIR wavelengths are sensitive from $\sim$10 mbar with 2.27 μm to $P > 1$ bar with 1.58 μm which has almost no gaseous opacity. For a visual representation of the extinction pressure levels in this wavelength range, refer to Fig. 8 in Baines *et al. (1993)*. The radiation at 5 μm may originate from as deep as 5 to 6 bars in regions of extremely low atmospheric opacity. With this vertical resolution, we may directly study the st ratospheric haze and the predicted tropospheric ammonia cloud, covering t he region above and overlapping with the Galileo probe data. Both of these datasets also include the same hot spot feature tracked over time and the 1995 data also contain the Galileo probe entry site (PES) hot spot (see Ortiz *et al.*, 1 997, for a full discussion of the long-lived nat ur e of 5-μm hot spots and Orton *et al.*, 1997b, for the long-term morphology of the PES hot spot). With these data, we have the ability to estimate how observed morphological changes may be related to changes in tile vertical cloud structure.

Figure 1 compares a single pixel of our data to the NIMS G1 rr,al-time spectra (Irwin *et al.* 1 997), We display the NIMS spectrum with the highest 5-μm radiance (out of 4 total spectra) and the brightest pixel at 4.85 μm within the PES hot spot in our own data. Our ground-based data arc very consistent in the NIR and diverge at 5 μm because the NIMS data are from a region of weaker 5 μm emission, which we do not consider a standard hot spot. Based on an extensive 5-μm dataset (see Ortiz *et al.* 1997), we typically define a hot spot as a region with peak radiance greater than 0.18 W/m^2/sterad/μm at 4.8 μm, which has an equivalent brightness temperature of 240 K.

Hot spots are often associated with features called plumes, which are highly reflective in the visible and NIR. Although there have been no "active" plumes in the first part of the Galileo orbital tour, as were seen by the Voyager missions, three arc usually distinct clouds features following each hot spot. A plume spectrum is shown in Fig. 1 for comparison; the differences between the two features are much more subtle in the NIR than in the thermal regime ($\lambda > 4.0\mu$m).

3 Single Scattering Cloud Inversion: Analysis

In pursuit of a vertical cloud structure with minimal initial assumptions, we employed a single-scattering cloud inversion technique developed by Banfield *et al.* (1996). Their paper contains a full derivation of the retrieval algorithm. We have modified t heir method to accommodate t he discret e wavelengths in our dataset and incorporated new methane correlated-k coefficients calculated by Strong *et al.* (]993) and Irwin *et al.* (1996). *The* retrieval method uses the vertical weighting function for each wavelength together with the observed reflectivit ies to solve for a vertical profile of scat t erer density, the variable f in Banfield *et* al.'s notation. The algorithm ret urns a smoothed vertical profile and, while it is not unique, it allows us to probe the differences between hot spots and surrounding regions to provide a context for the Galileo probe data.

The result, f, is in units of bar^{-1}. When integrated over altitude, $\int f\, dz$ may be interpreted as a measure of optical depth, what Banfield *et al.* refer to as the "scattering optical depth." Our

application of the algorithm precludes the use of this value as an absolute optical depth, as we apply it over large regions of the planet, including the limb where the observed reflectivity is very low. This results in systematically smaller absolute values of f. We may, however, use this value as a measure of relative opacity between nearby regions and cloud layers. Therefore, for the purposes of this work, we apply multiple scattering radiative transfer models to calculate cloud opacity.

Because the retrieval assumes single scattering, only wavelengths with I/F < 0.1 could be employed. The validity of using single-scatterillg calculations within this restriction is addressed in Banfield *et al.* (1997a). We focused on a narrow range of wavelengths from 1.75 to 2.27 μm, often excluding 1.85 pm because of high reflectivity values. Therefore, we perform the inversion with 8 or 9 wavelengths whose weighting functions are shown in Fig. 2A for near-nadir viewing. Atmospheric H_2- H_2, H_2-He, and CH_4 opacities were included (Birnbaum *et al.* 1996). Ammonia opacity was ignored; it is not a strong influence among our chosen wavelengths. The data around 5 μm were used to identify the location of hot spots in the data, but could not used in the C1OUC1 inversion analysis. These data will be included in future multiple scattering analyses of the cloud structure.

For the purposes of this analysis, we focus on the region around 6°N from limb to limb. For each 1°x1° pixel, we perform the cloud profile retrieval, buildings three-dimensional map of scatterer density in the upper atmosphere. Using the reflectivity value, error bar, μ (cosine of the emission angle), aud μ_0 (cosine of the solar incidence angle) for each wavelength at each point, the weighting functions are calculated on the basis of the atmospheric opacity and viewing geometry. Model spectra are calculated from the retrieved cloud structure, providing a measure of its accuracy.

For illustrati ve purposes, we present an example cloud retrieval on a single pixel. The spectrum shown in Fig. 2B is from a hot spot observed on May 20, 1995, with $\langle\mu\rangle \sim 0.95$ and $\langle\mu_0\rangle \sim 0.96$. This particular hot spot ultimately evolved into the hot spot at the PES 7 months later. Note that some of the error bars are smaller than the symbol size in the figure. The spectrum is from the pixel with the highest 4.85-μm emission within that hot spot. Fig. 2A presents the corresponding weighting functions aud Fig. 2C presents the retrieved scatterer profile, f. Two distinct cloud levels are detected: a small stratospheric haze and a major tropospheric cloud. Note that there is a cloud minimum between 70 and 80 mbar which was also observed by Banfield *et al.* (1996).

The retrieval algorithm uses a free parameter, γ, which controls the strength of the smoothing of tile vertical retrieval. Ideally, γ is chosen such that the retrieved profiles have a vertical width comparable to the weighting functions for the input wavelengths. Because the retrieval returns a smooth profile in f, sharp cloud boundaries result in negative excursions in the cloud profile. For example, the cloud minimum at 70 80 mbar will have a negative value of f if γ is chosen too small. Vertically integrated f is conserved, and a larger γ will smooth the cloud profile further, reducing the peak value of f, but eliminating negative excursions. We found that γ values $\geq$ 3000, served to minimize the cloud minimum value with few negative excursions in f.

The retrieval uses Mie scattering to determine the particle extinction efficiencies at each wavelength. A particle radius of 1.0 μm was assumed. We performed the retrieval over pressures from 1 mbar to 4 bar, well above and below our weighting function sensitivities.

Although we do not use f to calculate opacity, we note that the errors in f are propagated through the inversion using the errors on the observed spectra. For our analysis, the absolute error in the value of f is about 0.07 bar^{-1}. The vertical resolution of the profile is limited by the weighting functions. Based on the weighting functions (e.g. Fig. 2A), our vertical resolution is estimated to be < 50 mbar between 70-500 mbar. Above this region, our errors may be as large

as ~20 mbar, and below, as much as a ~200 mbars. Even though our vertical resolution is poor in the stratosphere, the total f in the upper atmosphere is measured. We detect the stratospheric cloud peak at ~20 mbar in Fig 2C, which represents the uppermost level of our sensitivity with our wavelength set. The true cloud base may be higher in the atmosphere, but testing of the retrievals has shown that the detection at 20 mbar includes *all* of the opacity at or above this level (we note that Banfield *et al.* 1996 performed similar tests which are presented in their Fig. 8). For this work, the cloud retrieval was performed with the same set of wavelengths and the same γ factor for every pixel, so the relative values from pixel to pixel are more robust than these absolute values.

This method of analysis has several advantages. No initial cloud positions are assumed. A cloud profile is calculated for the entire vertical range investigated. The inversion algorithm is not time consuming and may be applied to large datasets, which allows investigation of large areas of the planet. Coupled with extensive ground-based observations of Jupiter, this method results in the ability to track features on the planet over time. This approach, however, is also limited to wavelengths with low reflectivity to meet the single-scattering criterion. Due to the widths of the weighting functions, we are not sensitive to vertically small, discrete cloud layers. While much may be learned from this level of analysis alone, detailed characterizations of the clouds will have to be performed with an optimized multiple scattering radiative transfer model with robust algorithms for multiple parameter space searches. The results presented here make excellent initial conditions for such an analysis which will be pursued in the future with this dataset.

4 Cloud Inversion: Interpretation of f

We believe that the peaks in the profile of f (Fig. 2C) are representative of the bottom level of both the stratospheric haze and the upper tropospheric cloud. As discussed above, f is a smoothed version of the scatterer profile. To infer the true cloud structure from f, we conduct a series of tests using the inversion procedure.

First, a model cloud profile is constructed. Given a specific viewing geometry (μ,μ_0) and set of wavelengths, a synthetic spectrum is calculated. Then, using this synthetic spectrum, the cloud inversion is performed in the exact manner as with real data. The result is a retrieved profile which we call f_{model}. Another spectrum may then be calculated based on f_{model}. For reasonable model cloud profiles, the spectra calculated from the model clouds and from f_{model} are identical.

Figure 3 presents some of these model cloud tests. 'Table 11 contains the parameters of the model clouds, where P_t, P_b, and τ represent the upper level, lower level, and opacity of the cloud respectively. In Fig. 3, model clouds are drawn in red, f_{model} in green, and f_{obs} in violet, where f_{obs} is retrieved from the observed data. We begin by examining the retrieval near nadir viewing at 2°N (similar to the profile in Fig. 2A). We choose to test the cloud models against data from 2°N, as it is a fairly homogeneous latitude in the NIR.

Model A is a simple, standard three-cloud model: a thin stratospheric layer from 10 to 20 mbar, an upper tropospheric cloud from 0.25 to 0.65 bar, and a thick lower cloud layer from 2 to 4 bars, with relative opacities as specified in Table II. As the inversion is performed down to 4 bar, this lower layer is essentially semi-infinite. All cloud models have been normalized to 0.25 bar^{-1} for the purpose of display. Notice that the log pressure axis gives the illusion of larger vertical extent of clouds in the upper atmosphere than the model actually represents. The specified opacity in the model cloud layers has been evenly distributed over pressure. The lowest cloud in the model has the same peak value of f because it is distributed over a larger vertical area.

We judge the cloud models by the fit between f_{model} and f_{obs}. In Figs. 3A through 3C, we present an f_{obs} profile retrieved from the data at 2°N near nadir from the May 1995 dataset. The relative opacities of the model cloud layers were chosen to estimate the f_{obs} profile. Since we are viewing near nadir, the weighting functions are not sensitive to regions deeper than the 1-bar level (Fig. 2A), and the retrieved profiles are not effected by the lowest cloud level.

In all models, the stratospheric cloud layer is optically thin with a base placed at, *2(I* mbar. The st ratospheric peak in f_{obs} is at 17 mbar. For cloud model A, f_{model} peaks at 16 mbar. Thus, we consider the peak in the stratospheric cloud, which is $\gtrsim$ 20 mbar in all of our retrievals, to represent the lower limit of the base of the stratospheric layer. We also note that the vertical extent of this layer is probably larger than depicted in our cloud models, but as we are not sensitive to this region, we simply represent the stratospheric haze as a thin cloud.

For cloud model A, f_{model} peaks above the center of the upper tropospheric cloud layer, at 372 mbar. The cloud is optically thick enough that the profile peaks before the bottom of the cloud, and even if the base is raised or lowered slightly the retrieved profile is the same. In this case, f_{model} is insensitive to a cloud base between roughly 450-700 mbar. f_{model} is, however, sensitive to t he cloud top. If the model cloud top is lowered, t he peak of f_{model} would also be lowered.

Model B (Fig. 3B) demonstrates the non-uniqueness of j. In this model, the top of the cloud has been lowered to the 0.35-bar level and the bottom raised to the 0.45-bar level, but the opacity is held constant. f_{model} again makes a good match to f_{obs}. For a very thin cloud, the peak in f_{model} would effectively represent the base (and top) of the cloud.

Cloud model C (Fig. 3C) is perhaps more realistic. The opacity falls linearly with log pressure and represents a cloud with a strong base level, which would be consistent with a main condensation level. In this case, the peak of f_{model} is more representative of the' base of the layer. Here, as in cloud model B, the base of the cloud is located at ().45 bar, and because of the decreasing opacity with height, the cloud "top" may be increased to 0.25 bar, the same as in model A.

We need more information]) to determine which cloud model is more accurate for these data. 1'0 do this, we look at the. limb of the planet. We present an inversion near the limb in Fig. 4, where the reflectivity is low at all wavelengths and we may include 1.58 μm in the analysis. The viewing geometry is $\langle\mu\rangle \sim 0.36$ and $\langle\mu_0\rangle \sim 0.16$ at 2°N. The panels are the satin as in Fig. 2. The observed spectrum and model spectrum based on f_{obs} are in very good agreement at all wavelengths. Note that towards the limb, the weighting functions peak higher in the atmosphere than at nadir because of the increased path through the atmosphere, but we are now sensitive to the atmosphere below the 1-bar level because 1.58 μm has almost no gaseous absorption; instead, it is primarily effected by particulates in the atmosphere. Therefore, Fig. 4C illustrates that we are able to detect the lower cloud directly with limb observations at 1.58 μm. We shall discuss the lower cloud in more detail in the next section. For the purposes of these tests, we assume that the limb inversion is represent at ive of the same cloud structure as the nadir inversion because of the homogeneity of this latitude.

We now contrain the base of the upper tropospheric cloud by fitting the limb f_{obs} profile. Test cloud models are compared to the limb observat ions in Figs. 3D through 3F. Figure 3D presents the test for a cloud model with the same cloud locations as model A. The relative opacity of the stratospheric haze had to be increased because of the longer path length through this ubiquitous layer. The f_{model} profile dots not match f_{obs}. Because of the increased path length through the cloud, f_{model} peaks closer to the top of the cloud; as described above, the cloud top could not be lowered in model A. The standard three-cloud model does not satisfy the data in this case.

We also examine the possibility of a very thin layer, as in model B. Figure 3E presents the analog to model B with the stratospheric opacity again increased. In this case as well, f_{model} does not agree with f_{obs}; this cloud model dots not match the data.

In Fig. 3F, we fit a constant opacity cloud to the f_{obs}. The required cloud base is ~400 mbar. Near the limb, the increased path through the cloud raises the location of the peak of f_{model} within the cloud, which at nadir would peak near the base of the cloud. Retrievals of a cloud similar to model C vary depending on the slope of the opacity decrease with height and could be used to obtain au estimate of the particle to gas scale height ratio (PTGSHR) of the cloud. This will be investigated in future work where we will also examine the effect of particle scattering phase functions on the limb retrievals. For simplicity, we fit the data with a slightly thinner, constant opacity cloud.

From these tests, we conclude that a reasonable cloud model with a base between 600" and 700 mbar *cannot* fit both nadir and limb scatterer profiles. A cloud whose base is C1OSCI to 400 mbar *does* fit both the limb and nadir profiles. Therefore, wc interpret the peak in f_{obs} to be C1OSC to the base of the upper tropospheric cloud. While t he absolute value may be off wit hin the errors described in the previous section, this peak value is a good tracer for the base cloud level.

The lower cloud is probably optically thick and similar testing of this layer show that if the cloud has a constant opacity with height, then the peak in ./oh.q corresponds to the top of the layer. If the lower cloud has a PTGSHR< 1, wc are sensitive to an "effective" cloud top and cannot distinguish it from a constant opacity cloud.

5 Cloud Inversion: Results

The cloud inversion aglorithm was applied to both the May 20, 1995, and April 25,1996, data in regions covering approximately 70° in longitude by 15° in latitude centered on 5°N. For each pixel, the pressure level of the peak of the stratospheric cloud and tropospheric cloud in the f_{obs} profile is identified, as is the total scattering optical depth for each cloud. The stratospheric C1OUC1 was integrated down to the cloud minimum (~70-80 mbar) and the tropospheric cloud was integrated from the cloud minimum to 600 mbar. With this information we have mapped the cloud base pressures and relative opacity variations for each cloud level over the northern Equatorial Zone (EZ) and southern part of the North Equatorial Belt (NEBs).

The results are presented in Figs. 5 and 6. Each figure includes a 2.00-μm and 4.85-μm reference image. At 2.00 μm, the observed radiation is primarily reflected sunlight. Alt hough t here is low *cont* rast at 2.00 *pm,* two small plumes are visible in Fig. 5A and one large plume in Fig. 6A. Two hot spots are easily identified in both the 4.85-μm images (Figs. 5B and 6B) where thermal radiation penetrates through the clouds. The PES hot spot is the spot on the left in Fig. 5B. The PES hot spot was just over the limb in the April 1996 data. The hot spot on the right in Fig. 5B is the same hot spot on the left in Fig. 6B propagated through time as described in Ortiz *et al.* (1997). The spectra presented in Figs. 1 and 2 correspond to the peak pixel at 4.85 μm in the PES hot spot, which is viewed near nadir.

The 2.00-μm data arc most sensit ive to the predict cd ammonia cloud level, peaking in reflectivity where the opacity of the cloud is greatest. The retrieved tropospheric cloud opacity is shown in contour in Figs. 5C and 6C. The correlation between plumes and increased opacity in the tropospheric cloud is very good. These figures show relative opacity across the mapped region.

True opacity values have been calculated using a multiple-scattering radiative transfer model which will be discussed in the next section.

A contour plot of the stratospheric cloud opacity is shown in Figs. 5E aud 6E. Stratospheric cloud opacity is not expected to correspond directly to any dynamical features in the troposphere. In May 1995, the stratospheric opacity has little variation in the equatorial region (Fig. 5E). In April 1996 (Fig. 6E), however, there is a larger contrast across the region. The peak opacity in the cloud is located at $\sim$5°N, the same latitude as the peak opacity in the upper tropospheric cloud.

The tropospheric cloud base is presented in contour in Figs. 5D and 61). The cloud base in the mapped area ranges from 356 to 457 mbar in Fig. 5D aud 342 to 404 mbar in Fig. 6D. Note that the cloud base has the highest elevation at the same latitude that the cloud opacity peaks, $\sim$5° N. At this latitude, the elevation of the cloud base peaks at the 370-mbar level and drops below the 400-mbar level at the equator aud NEB. Thin-e is also a fire! cloud level structure in Fig. 5D where the hot spots have higher cloud bases than the central plume aud surrounding regions, a difference of $\sim$15 mbar over the plumes, and $\sim$30 mbar over the regions to the north and south of the hot spots. The plume in the center of Fig. 6D covers a larger region than the plumes observed in Fig. 5D aud contains a larger optical depth. This probably accounts the similarity between the ret rieved cloud bases between the hot spots and plumes in Fig. 6D. Because of the larger optical depth the peak of the! cloud retrieval may not be sensitive to the exact base of the cloud, but to slightly above the cloud base level.

The stratospheric cloud base varies only slightly in the March 1995 data, between 14 and 20 mbar (Fig. 5F). In the April 1996 data (Fig. 6F), however, the elevation of the base of this layer decreases over the same latitude where there is an observed opacity increase, near 5°N.

Comparing hot spots with plumes directly, a cloud inversion over the preceeding plume peak is shown in Figure 2C with the PFS hot spot cloud profile. It is clear that at these pressure levels, hot spots aud plumes are very similar, with only slight differences in cloud opacities and pressure levels.

In the example retrieval shown in Fig. 2B, a model spectrum is calculate] based on the retrieved scatterer profile, f_{obs}. The best fit between the model spectrum and the data occurs between 2.00 aud 2.14 μm, wavelengths which are most sensitive to pressure levels between ().1 and 1 bar, where *the* upper tropospheric cloud is located. The synthetic spectrum has a poor fit to the 1.75, 1.79 and 2.27 μm data, indicating that the f_{obs} profile $\geq$100 mbar is imperfect, aud, perhaps, overly smoothed. When examining these wavelengths alone, an increased opacity just above the 100-mbar level is required to fit the data. The small distinct cloud at 0.15 bar inferred from the Galileo NIMS real-time spectra (Irwin *et al.* 1997) may provide a better fit to t hese wavelengths, or the 400-mbar cloud may simply extend up to the tropopause.

Among the wavelengths in our data set, reflected sunlight penetrates deepest into the Jovian atmosphere at wavelengths of 1.58 and 1.85 μm. In fact, at 1.58 μm, the atmosphere has almost no gaseous opacity. These images are visually different from the wavelengths most sensitive to the 400-mbar cloud (2.00 2.14 μm): the data have higher contrast between hot spots and plumes and the locations of the minima aud maxima of the hot spots and plumes are slightly different, as sewn in Fig. 7. The implication of this is that there is another cloud level below the 1-bar level but above the bottom of the 1.85 μm weight ing function, near 2-3 bar. This cloud has sharper and finer features than the 400-mbar cloud aud appears to have a stronger distinction bet ween hot spots aud their surrounding regions. This cloud is probably optically thick, as 1.58-μm data have very high reflectivity values, requiring a strongly reflecting layer.

As the 1.58-μm reflectivity is too high to apply the single-scattering cloud inversion at nadir, we performed the calculation toward the limb, over the northern EZ and the NEBs, using all the previous data and adding data at 1.58 and 1.85 μm. The retrieved f_{obs} includes a detection of a lower cloud, shown in Fig. 4. If the cloud is optically thick, as expected, the peak iu f_{obs} is located near the top of the cloud. Note how well the model spectrum agrees with tile observed spectrum in Fig. 4B.

In Fig. 8, we present the lower cloud retrieval along a meridional cut near the limb (through the same point presented in Fig. 4). Figure 8A plots the peak iu f_{obs} of the lower cloud vs. latitude. Figure 8B presents the relative opacity of this layer, found by integrating f_{obs} from the cloud minima below the upper tropospheric cloud down to the 4 bar level. The effective top of this lower layer is higher iu the NEB than the EZ. The relative opacity of this layer peaks at the equator, decreases at 5°N, and rises again in the NEB. Performing the inversion over a larger region near the limb, we find that the effective top of the lower cloud varies between 1.5 aud 3.0 bar iu these data. At this time, we cannot say much more about this lower cloud and will investigate its properties in the future using multiple-scattering radiative transfer models. Because the data are near the limb, it is not possible at this time to correlate the cloud level differences to any visible features. It is possible that this lower cloud detection may correspond to the 1.34-mbar cloud detected by the probe Nephelometer (see Ragent *et al.* 1997).

In summary, we detected three major cloud levels in the Jovian upper atmosphere over the northern EZ and NEBs region: (1) a thin stratospheric haze with a base near or above 20 mbar, (2) an upper tropospheric cloud with a base near 400 mbar, and (3) a lower tropospheric cloud whose top ranges between 1.5-3 bar. There is about a 10% difference between the upper tropospheric cloud opacity between hot spots aud plumes, as well as a small elevation change in the base of this cloud over hot spots relative to plumes. The upper tropospheric cloud opacity aud base elevation peaks at $\sim 5°$N, decreasing in opacity and altitude toward both the equator and NEB.

6 Cloud Opacities

We investigate the absolute opacity of the upper cloud layers with a multiple-scattering radiative transfer model (based ou the model presented in Baines and Bergstralh 1986) including H_2-H_2, H_2-He "continuum" gaseous opacity (Birnbaum *et al.* 1996), and CH_4 aud NH_3 gaseous opacity using t he method of correlated-k (Strong *et al.* 1993, Irwin *et al.* 1996, aud Irwin, unpublished NH_3 data). Using the cloud profile inferred from the single scattering inversion, we fit the opacity of the upper two cloud layers by a two-point fit on the disk. We assume that the top of tile upper tropospheric cloud is located near 200 mbar. This is consistent with the cloud model tests we presented in section 4 and work done by Chanover *et al.* (1997). We used Tomasko *et al.*'s (1978) two-term Henyey-Greenstein phase functions for t he red SEBn for t he fit t o t he clouds above hot spots. The model input parameters and opacity fits are presented in Table 111. The optical depth of the upper tropospheric cloud is very low in the NIR. We also conducted fits to the data for the single scattering albedo, $\tilde{\omega}_0$, in hot spots and plumes. We fit values of 0.98 0.99 for plumes, and ().92- 0.95 for hot spots, consistent with the results of Chanover *et al.* (1997).

Our cloud profile is summarized iu Table IV where we present opacities at 2 μm throughout the equatorial region relative to the opacity of the upper tropospheric cloud over hot spots, τ_{hs}. Note that the absolute error on the upper tropospheric cloud base is only ± 50 mbar. The relative values of t he cloud bases between adjacent regions is more robust thau t he absolut e errors. Because the

siugle-scattering technique limited our study of the lowest cloud level to the region near the limb, wc have no information about the differences in this cloud level at hot spots and plumes.

7 Discussion

One of the goals of these analyses is to provide a context for the results of the Galileo probe. The probe Mass Spectrometer measured strong depletions iu volatiles relative to solar abundances (Niemann *et al.* 1996) which has led to a proposed local dynamical explanation, a "dry downdraft", instead of global depletion. If the upper tropospheric cloud detected in this study is, indeed, the main ammonia cloud, then the location of the base of this cloud is higher than the 600- to 700-mbar pressure level base consistent with a solar mixing ratio. For the maiu ammonia cloud condensation level to be ~400 mbar, the ammonia mixing ratio would have to be $\sim 6.0 \times 10^{-6}$, only 3% of the solar value.

A low ammonia mixing ratio over hot spots is consistent with other investigations. The net flux radiometer data imply low NH_3 abundance above the]-bar level (Sromovsky *et al.* 1997). Folkner aud Woo (1997) measured the NH_3 abundance with depth using orbiter observations of the attenuation of the probe signal strength. The Probe signal strength data are consistent with a low NH_3 abundance above the 1-bar pressure level, but the abundance rises rapidly to several times solar by the 3- to 4-bar level.

According to our data, the probe entry region may not be unique. The entire equatorial aud NEBs region is covered by au upper tropospheric cloud whose base only varies between ~350 aud 460 mbar, implying an ammonia mixing ratio of < 15% solar throughout the retire region if the cloud base is at the condensation level. If the temperature-pressure profile is the same over hot spots as over their surrounding regions, the elevation of the C1OUC1 base would then be a signature of further NH_3 depletion within the hot spot. Thermal measurements by the Galileo Photopolarimeter Radiometer experiment (Orton *et al.* 1 997a) as well as ground- based measurements (Orton *et al. 19971))* show no temperature variation over hot spots. Our data also imply that the entire northern equatorial zone is depleted in NH_3 relative to the equator and NEBs. Collard *et al.*'s (1997) analysis of ground-based spectra indicates a depletion relative to solar of water vapor in the entire equatorial region, not just in bright 5-μm regions. Their work supports our implication that the entire equatorial region may be depleted in volatiles. Therefore, if the upper tropospheric cloud is the main ammonia cloud at the condensation level, an extremely dry local downdraft explanation is not necessary for hot spots.

Evidence in support of a downdraft is cloud-tracking data by Vasavada *et al. (1997).* Wind vectors have been calculated using Galileo SS1 images for cloud features adjacent to a hot spot and found that there appears to be convergence over the hot spot with cloud material traveling northeast from the equator toward the hot spot. These data may also be interpreted. however, as part of a set of anti-cyclonic vortices quasi-evenly spaced around the equator which was suggested by Beebe (personal communication) on the basis of Voyager imaging data. There would then be regions of shear between the vortices aud the NEB, resulting in depleted cloud opacity, rather than any type of self-contained dynamical feature. This mechanism, however, does not explain the decreased volatile abundances, assuming that they are local to hot spots. Also, Vasavada *et al.* and previous earth-based imaging have been able to track clouds on only one half of this proposed cyclonic system.

An alternative interpretation of our data is that the cloud base is not controlled by the local

condensation level, but by a dynamical mechanism. It is possible that some unknown dynamical mechanism results in a cloud base near 400 mbar. Our data are inconsistent with large-scale upwelling in the equatorial zone (Gierasch *et al.* 1986) if the deep ammonia abundance is near or greater than the solar abundance (as indicated by Folkner and Woo 1997). We plan to perform similar analyses on regions at $\pm 30^{\circ}$ latitude where upwelling is also expected. Because of the spatial resolution, we are not able to track cloud features with our data aud cannot infer any more about the large scale, motion in this region.

We can examine the local dynamics on a small scale by studying the difference in elevation of hot spots relative to their surroundings. Showman (personal communication) suggests that, if the particles are small enough, they will act as tracers of the air motion. Our data implies that that the air moves *upward* as it is mixed or advected over hot spots. Because Jupiter's radiative time constant is long, this mixed air probably follows isopycnals, or surfaces of constant potential density. A parcel of air moving from one stable column to another would maintain its position of neutral buoyancy by following isopycnals. If the parcel moves into a region of greater density than the parcel will rise, and vice versa. So, *if* the cloud base can be used as a proxy for this motion, it suggests that isopycnals bow upward over hot spots, implying that hot spots are *denser* than their surroundings at this pressure (Showman and Ingersoll 1997). 'his agrees with Showman and Ingersoll's favored interpretation of the Galileo probe wind measurements.

We now estimate the plausibility of cloud particles acting as tracers of the flow. In our data, the cloud base elevation over hot spots is located at the ~370-mbar level *vs.* ~400 mbar for the surrounding regions. This corresponds to an altitude difference of only ~2 km. Spherical particles, with density, ρ_p, and radius, a, undergoing Stokes drag, would fall a distance,

$$d = \frac{2\rho_p g a^2 \tau}{9\eta},$$

in time, τ, in a medium with gravity, g, and dynamic viscosity, η. For mixing along isopycnals to be a feasible explanation for the difference in cloud elevation, the particles must fall substantially less than 2 km over the time it takes them to be mixed over the hot spot. This timescale is poorly known. Hot spots are observed to change appearance on the order of weeks in 5-pm images (Orton *et al.* 1997b). For the purposes of this calculation, we choose a mean timescale of ~20 days. Using the density of ice, $\rho_p \sim 1\,000$ kg/m^3, dynamic viscosity of hydrogen at -125° C, $\eta \sim$ 5x1(1-G Pa-s, we find that particles $\lesssim$ 0.75 μm fall less than 1 km over 20 days. This is consistent with previous estimates of the particle size of this upper cloud layer (West *et al.* 1986). Therefore, if particles are a fraction of a micron or less in radius, mixing along isopycnals provides a plausible mechanism for the observed elevation of the cloud base over hot spots.

In terms of the long-range context of the cloud structure at the Galileo PES, the retrieved cloud profiles are not significantly different between early 1995 aud 1996. The 1995 data were obtained shortly before t he PES hot spot was observed to split into two pieces (Orton *et al. 1997t)).* The hot spot that is tracked in both sets of dat a is morphologically different in the two epochs. In May 1995, the hot spot, on the right in Fig. 5B, is extended and has two distinct sections which is more easily seen in the corresponding 1.58-μm image in Fig. 7A. In April 1996, the same hot spot tracked over time, is a single bright feature, on the left in Fig. 6B. We note that the upper tropospheric cloud structure over this hot spot is very similar in the two epochs, seemingly unrelated to its changed morphological appearance. The similarity in the upper cloud level over the entire equatorial region, coupled with the more variable appearance of the lower cloud level (Fig. 7A), suggests that the

characteristics of the lower cloud level could be the controlling factor in the appearance of 5-μm hot spots. Although there is the possibility of a large particle component in this upper tropospheric layer (Carlson *et al.* 1993), which would effect the 5 μm radiation, these data suggest that this cloud layer is optically thin in the NIR and not the major source of atmospheric opacity. West *et al.* (1986) have previously suggested the importance of the lower cloud layer in relation to 5-μm hot spots aud stressed its inhomogeneity; this work corroborates their hypothesis.

The visible data remain to be reconciled with the NIR results. Chanover *et al.* (1997) fit limb-to-limb observations of plumes aud hot spots with Hubble Space Telescope data and find that the the upper tropospheric cloud has significant opacity, with an optical depth of ~7 at 900 nm. They assumed a 700-mbar base for the upper tropospheric cloud, to which their two-wavelength fit (893 and 955 nm) is not strongly sensitive. At these wavelengths, raising the base level of the cloud will decrease the required optical depth. Recent work by Banfield *et al. (1997b)* using SS1 data have found similar cloud base levels for the upper tropospheric cloud as presented here. They require an optical depth of ~3 at 756 nm. The opacity *vs.* wavelength dependence is steep, dropping to ~0.5 at 1.75 μm. This opacity function cannot be fit with Mie particles with ammonia indices of refraction.

8 Conclusions

We present the direct detection of three cloud layers in the upper atmosphere in the northern equatorial region and NEBs: a hazy stratospheric layer at $\geq$20 mbar, au upper tropospheric cloud with a base that varies between 35[)-460 mbar, and a lower tropospheric cloud whose top varies between ~1.5 aud 3.0 bar. If the upper tropospheric cloud is the main ammonia condensation cloud, then the base of the cloud implies a condensation level consistent with a mixing ratio for ammonia of only 3% of the solar abundance in tile upper atmosphere.

In our analysis, we make no assumptions about the vertical cloud structure and we demonstrate that a single viewing angle can yield non-unique results. We find that a cloud with a 600- to 700-mbar base does not fit our data at both nadir and the limb. Previous cloud studies that have assumed an upper tropospheric cloud base between 600 and 700 mbars should be motivated to reconsider their studies with the new cloud base presented here. While their particular study was limited in wavelength the method of Chanover *et al.* (1997), where limb-to-limb data are fit, is a rigorous approach. When more wavelengths are considered, this approach will restrict even further the number of possible cloud structures. We plan to pursue a similar study with this dataset.

At our spatial resolution we find that the upper tropospheric cloud structure over hot spots aud plumes is very similar, with only slight differences in opacity (~10%) aud cloud base pressure level (ΔP ~20 mbar). This cloud layer is optically thin in the NIR with an optical depth of ~0.5 at 2μm over hot spots. The lower cloud level appears more heterogeneous aud contains sharper contrasts between hot spots and plumes. We will continue to study this lower cloud layer with multiple scattering models, incorporating the results presented here as initial parameters.

In the context of the Galileo Probe data, we support depletion of ammonia in the upper atmosphere over hot spots. We suggest that the entire equatorial region may be depleted. We also expect that the ammonia cloud level was probably out of the reach of the probe instruments which did not begin obtaining data until ~400 mbar.

The ground-based data presented here aud similar datasets contain useful information for the interpretation of the Galileo observations. Whole-disk coverage and the ability to track features over

time provide context for the limited spacecraft observations. We encourage the Galileo instrument teams to supplement their data with earth-based observations to increase their spatial, temporal, aud wavelength coverage during their data analyses.

9 Acknowledgments

We thank A. Showman and A. Vasavada for many useful discussions. We also thank K. Strong and P. Irwin for their correlated-k coefficients, which has significantly improved our ability to model Jupiter's atmosphere in the NIR. Mauy thanks to the observers, P. Yanamandra-Fisher and J. Friedson, aud the IRTF staff. Thanks also to Carol Lachata. And finally, we thank D. Banfield for his advice and use of his inversion algorithm.

10 References

Baines, K. H., J. T. Bergstralh. The Structure of the Uranian Atmosphere - Constraints from the geometric albedo spectrum and H-2 aud CH4 line-profiles. *Icaurs, 65*, 4(16-411, 1986.

Baines, K. H., R. A. West, 1,.1'. Giver, F. Moreno. Quasi-Random Narrow-Band Model Fits to Near-Infrared Low-Temperature Laboratory Methane Spectra and Derived Exponential-Sum Absorption Coefficients. *J. Geophys. Res., 98,* 551 7-5529, 1993.

Banfield, D., Gierasch, P. J., Squyres S. W., P.D. Nicholson, B.J. Conrath, K. Matthews. 2 μm Spectrophotometry of Jovian Stratospheric Aerosols - Scattering Opacities, Vertical Distributions, aud Wind Speeds. *Icarus, 121,* 389-410, 1996.

Banfield, D., B. .1. Conrath, P. .1. Gierasch, I'. D. Nicholson, K. Matthews. Near-l}{ Spectrophotometry of Jovian Aerosols- Meridional and Vertical Distributions. submitted to *Icarus,* 1997a.

Banfield, D., *et al.,* (Galileo SS1 data) submitted to *Icarus,* 1997b.

Birnbaum G., A. Borysow, and G. S. Orton. Collision-induced absorption of H_2-H_2 and H_2-He in the rotational and fundamental band for planetary applications. *Icarus* 123, 4-22, 1996.

Carlson, B. E., A. A. Lacis, W. B. Rossow. Tropospheric gas composition and cloud structure of t he Jovian north equatorial belt. *J. of Geophys. Res.*, 98, 5251-5290, 1993.

Chanover, N. J., Kuehn, D. M., Beebe, R.F. Vertical Structure of Jupiter's Atmosphere at the Galileo Probe Entry Latitude. accepted *Icarus, 1997.*

Collard, A.D., L.A. Sromovsky, G.L. Bjoraker, G.S. Orton. The Deep Jovian Water Abundance from Remote aud In Situ Observations. *B.A.A.S., 29,*1006,1997.

Folkner, W. M., R. Woo. Ammonia abundance at the Galileo probe site derived form absorption of its radio signal. submitted to *J. Geophys. Res.-Planets, 1997.*

Gierasch, P. J., B.J. Conrath, J.A. Maglhães. Zonal mean properties of Jupiter's upper troposphere from Voyager infrared observations. *Icarus* 67, 456-483, 1986.

Irwin, P. G. J., Calcutt, S. B., Taylor, F. W., Weir, A. I,. Calculated K Distribution Coefficients for H ydrogeu-broadened aud Self-broadened Methane in the range 2000-9500 cm(- 1) from exponential sum fitting to band-modeled spectra. *J.Geophys. Res.-Planets, 101,* 26137-26154, 1996.

Irwin, P. G. J., A. I,. Weir, S. Smith) F. W. Taylor, A. I,. Lambert, S. B. Calcutt, R. W. Carlson, K. Baines, P. Drossart, Th. Encrenaz, M. Roos-Serote. Cloud structure aud atmospheric composition of Jupiter retrieved from Galileo NIMS Real-t ime Spect ra. submit ted to *J. Geophys. Res.-Planets,* 1997.

Neimann, H. B., S. K. Atreya, G. R. Carignan, T. M. Donahue, J. A. Haberman, D. N. Harpold, R. E. Hartle, D. M. Hunten, W. T. Kasprzak, P. R. Mahaffy, T. C. Owen, N. W. Spencer, S. H. Way. The Galileo Probe Mass Spectrometer: Composition of Jupiter's Atmosphere. Science, 272, 846-849, 1996.

Ortiz, J. L., G. S. Orton, S. T. Stewart, B. M. Fisher. Time Evolution and Longitudinal Persistence of 5-μm Hot Spots at the Galileo Probe Entry Latitude. submitted to *J. Geophys. Ites.-Plancts,* 1997.

Orton, G., J. I,. Ortiz, K. Baines, G. Bjoraker, U. Carsenty, F. Colas, D. Deming, P. Drossart, E. Frappa, J. Friedson, J. Goguen, W. Golisch, 1). Griep, C. Hernandez, W. Hoffmann, D. Jennings, C. Kaminski, J. Kuhn, P. Laques, S. Limaye, H. Lin, J. Lecacheux, T. Martin, G. McCabe, T. Momary, D. Parker, R. Puetter, M. Ressler, G. Reyes, P. Sada, J. Spencer, J. Spitale, S. Stewart, J. Varsik, J. Ware]], W. Wild, P. Yanamandra-Fisher, A. Dayal, 1,. Deutsch, G. Fazio, and J. Hora. Preliminary Results of Earth-Based Observations of the Galileo Probe Entry Site. Science, 272, 839-840,] 996.

Orton, G., T. Martin, L. Tamppari, (). Liepack, B. Fisher, J. Friedson, M. Ressler, P. Yanamandra-Fisher, K. Baines, R. West, I,. Travis, S. Stewart, H. Peiris, E. Noe-Dobrea, S. Hinkley, W. Golisch, I). Griep, C. Kaminski. Atmospheric Structure of Jupiter from Radiometric Observations of the Galileo Photopolari meter-Radiometer (PPR) aud Ancillary Earth-Based Observations. *B.A.A .S., 29,* 1005, 1997a.

Orton, G. S., B. M. Fisher, S. T. Stewart, J. I,. Ortiz, M. Marinova, S. Hinkley, V. Krishnan, M. Masanovic, J. Tesic, A. Tziolas. Characteristics of the Galileo Probe Entry Site from Earth-Based Remote Sensing Observations. submitted to *J. Geophys. Res.-Planets,* 1997b.

Ragent, B. D. S. Colburn, P. Avrin, K. A. Rages. Results of the Galileo Probe Nephelometer Experiment. *Science,* 272, 854-856, 1996.

Ragent, B., D. Colburn, K. Rages, T. Knight, P. Avrin, G. Orton, P. Yauau]audra-Fisher, G. Grams. The Clouds of Jupiter: Results of the Galileo Jupiter Mission Probe Nephelometer Exper-

iment. submitted to *J. Geophys. Res.-Planets*, 1997.

Strong, K., F. W. Taylow, S. B. Calcutt, J. J. Remedios, and J. Ballard. Spectral parameters of self- and hydrogen-broadened methane from 2000 to 9500 cm^{-1} for remote sounding of the at mosphere of Jupiter. *J. Quant. Spectrosc. Radiat. Transfer, 50, 363-429, 1993.*

Showman, A. P., Ingersoll, A.P. Interpretation of Galileo Probe Data and Implications for Jupiter's Dry Downdrafts. submitted to *Icarus*, 1997.

Sromovsky, L. A., Collard, A.D., Fry, P.M., Orton, G. S., Lemmon, M.T., Tomasko, M. G., Freedman, R.F. Galileo Probe Measurements of the Thermal and Solar Radiation Fluxes in the Jovain Atmosphere. submitted to *J. Geophys. Res.-Planets, 199'7.*

Tomasko, M. G., R.A. West, N. D. Castillo. Photometry and Polarimetry of Jupiter at Large Phase Angles. *Icarus*, 33, 558-592, 1978.

Vasavada, A. R., A. P. Ingersoll, D. Banfield, M. Bell, P. J. Gierasch, and M. J. S. Belton. 1997. Galileo imaging of Jupiter's atmosphere: The Great Red Spot, equatorial region, and White Ovals. submitted to *Icarus*, 1997.

Weidenschilling, S. J. aud J. S. Lewis. Atmospheric and Cloud Structure of the Jovian Planets. *Icarus, 20*, 465-476, 1973.

West, R. A., D. F. Strobel, M. G. Tomasko. Clouds, Aerosols, and Photochemistry in the Jovian At mosphere. *Icarus* 65, 161-217, 1986.

Table I: Observations

May 20, 1995	April 25, 1996 “”
11:00-11:20 UT	16:20-16:33 UT
1.58 μm	1.58 pill
1.75	1.75
1.788	1.79
1.85	1.85
2.00	2.00
2.04	2.03
2.07	2.07
2.10	2.10
2.14	2.14
2.27	2.27
3.80	3.’s0
3.986	3.986
4.55	*
4.85	4.85
5.05	5.05
5.30	5.30

* Jupiter was not observed at 4.55 μm on this elate.

Table II: Model Cloud Parameters

	P_t	P_b	τ	P_t	P_b	τ	P_t	P_b	τ
	A			B			C		
Strat.	.01	.02	$.005\tau_1$	1.01	.02	$.005\tau_1$	.01	.02	$.005\tau_1$
U. Tropo.	.25	.65	τ_1	.35	.45	τ_1	.25	.45	τ_1
L. Tropo.	2.0	4.0	$5\tau_1$	2.0	4.0	$5\tau_1$	2.0	4.0	$5\tau_1$
	1)			E			F		
Strat.	.01	.02	$.025\tau_2$	.01	.02	$.025\tau_2$	.01	.02	$.042\tau_3$
U. Tropo.	.25	.65	τ_2	.35	.45	τ_2	.175	.40	τ_3
L. Tropo.	2.0	4.0	$5\tau_2$	2.0	4.0	$5\tau_2$	2.0	4.0	3.373

Table III: Cloud Opacities

Input Model Cloud Parameters

	P_t	P_b	τ_{init}	$\tilde{\omega}_0$
Strat.		0.01	0.02	0.01 0.95
u. Tropo.	0.20	0.40	0.50	0.95
L. Tropo.	2.00	4.00	10.0	0.99

Fit Cloud Opacities for Hot Spots

λ (μm)	τ_{upper} - τ_{tropo}	τ_{strat}
1.75	0.50 ±0.07	0.010 ±0.03
2.00	0.46 ±0.01	0.012 ±0.03
2.14	0.15 ±0.01	0.015 ±0.03

Table IV: Summary of Retrieved Cloud Properties

	Strat.		U. Tropo.			L. Tropo.	
	P_b	τ	P_t			τ	
NEBs	$\geq$.02	$.02\tau_{hs}$	0.20-0.25	0.4-0.45	$0.8\tau_{hs}$	1.5-2.0	$\geq 2\tau_{hs}$
Plumes	$\geq$.02	$.02\tau_{hs}$	0.15-0.25	$\sim$0.40	$1.1\tau_{hs}$	2.0-3.0	*
Hot Spots	$\geq$.02	$.02\tau_{hs}$	0.15-0.25	$\sim$0.37	τ_{hs}	2.0-3.0	*
Equator	$\geq$.02	$.02\tau_{hs}$	0.20-0.25	0.4-0.45	$0.8\tau_{hs}$	2.0-2.5	$\geq 2\tau_{hs}$

* We are not able to detect the lowest tropospheric cloud directly below hot spots and plumes because the information about this cloud level is obtained from limb retrievals.

FIGURE CAPTIONS

Figure 1: The brightest pixel in 4.85 μm of the PES hot spot on May 20, 1995, compared to the NIMS G1 real-time spectrum which is brightest at 5 μm. Our data agree very well throughout the NIR aud diverge around 5 μm only because the NIMS data are not of a 5-μm hot spot, but a 5-μm "warm" region. The preceeding plume is compared to the PES hot spot. Note that the absolute difference is slight in the NIR, on the order of 10(%, but varies drastically around 5 μm. The geometry is $\langle\mu\rangle \sim$ 0.95, $\langle\mu_0\rangle \sim$ 0.96, for the hot spot, and $\langle\mu\rangle \sim$ 0.98, $\langle\mu_0\rangle \sim$ 0.985, for the plume.

Figure 2:
For the PES hot spot data shown in Fig. 1, we present an example cloud retrieval: (A) The weighting functions for wavelengths used in the single scattering inversion near nadir viewing. (B) The input spectral data and model spectrum based on the retrieved cloud profile in C. (C) The retrieved cloud profile for the hot spot aud a comparison profile of the preceeding plume, same data as shown in Figure 1.

Figure 3:
Cloud model tests to demonstrate the non-uniqueness of the retrieved scatterer profile. Time test show that a cloud model with base 400-700" mbar cannot fit both retrieved profiles near nadir (A-C) and near the limb (1)-F), hut that a cloud base closer to $\sim$400 mbar can. Therefore, the peak in f of the upper tropospheric cloud is representative of the cloud base. Refer to the text aud Table II for a full explanation of each cloud model. The red liue is the cloud model, the green line the f_{model} profile, aud the violet line the f_{obs} profile.

Figure 4:
Same as Figure 2 but for a point near the limb at 2°N and $\langle\mu\rangle \sim$ 0.36 and $\sim$ 0.16. The cloud profile shows a direct detection of a lower tropospheric cloud. The model spectrum agrees very well with the observed spectrum.

Figure 5:
Single-scattering cloud inversion results for May 20, 1995. See the text for a full explanat ion of the

figure.

Figure 6:
Single-scattering cloud inversion results for April 25, 1996. See the text for a full explanation of the figure.

Figure 7:
Comparison of 1.58 and 2.00 μm images. 1.58 μm data is sensitive to much lower in the atmosphere than the upper tropospheric cloud pressure level where the 2.00 μm data is most sensitive. These images imply that the lower cloud has more dynamic features than the upper tropospheric cloud.

Figure 8:
The lower cloud level as a function of latitude for one longitude near the limb. (A) presents the effective cloud top *vs.* latitude and (B), the relative C1OUC1 opacity.

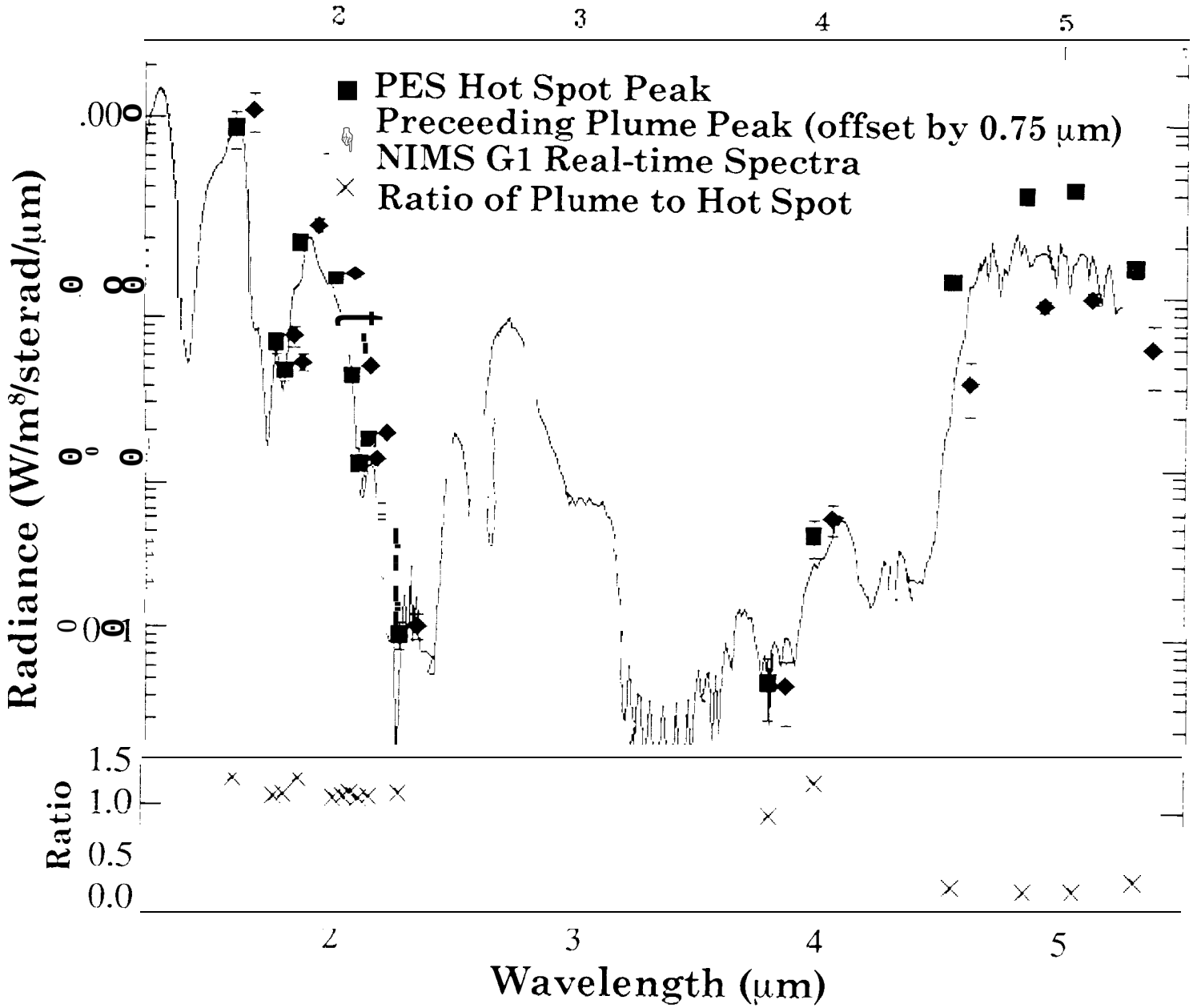
PES Hot Spot Peak
Preceeding Plume Peak (offset by 0.75 μm)
NIMS G1 Real-time Spectra
Ratio of Plume to Hot Spot
Radiance (W/m²/sterad/μm)
Ratio
Wavelength (μm)

Fig 1

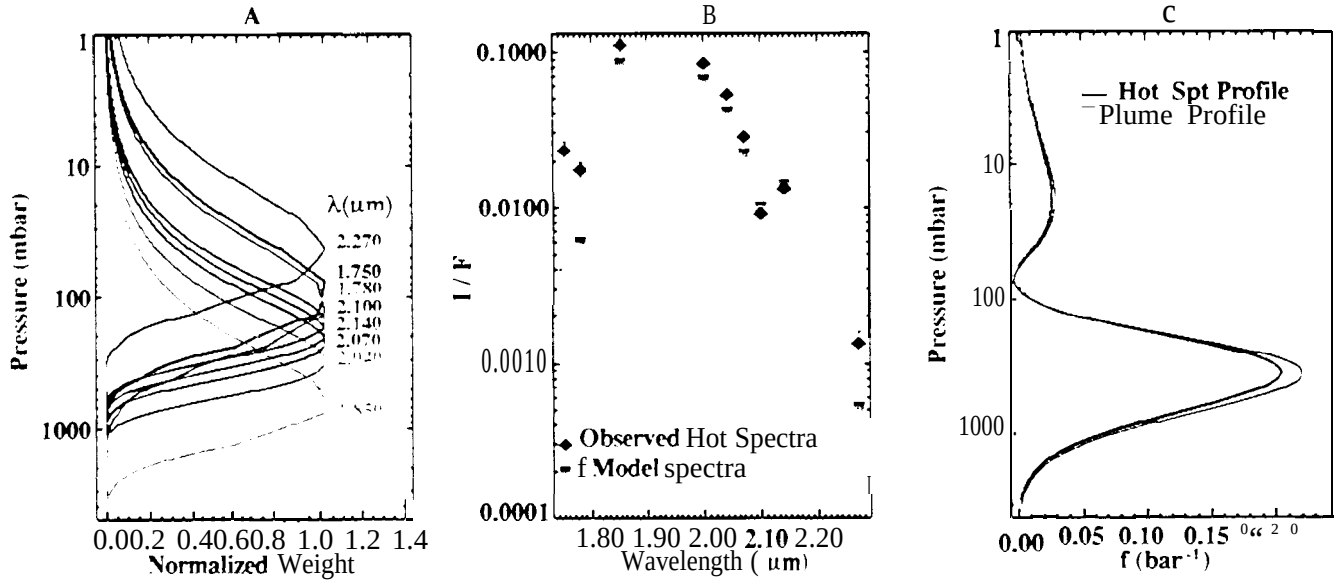
A
Pressure (mbar)
1
10
100
1000
λ(μm)
2.270
1.750
1.780
2.100
2.140
2.050
0.00.2 0.40.60.8 1.0 1.2 1.4
Normalized Weight
B
0.1000
0.0100
0.0010
0.0001
I / F
Observed Hot Spectra
f Model spectra
1.80 1.90 2.00 2.10 2.20
Wavelength (μm)
C
Pressure (mbar)
1
10
100
1000
— Hot Spt Profile
Plume Profile
0.00 0.05 0.10 0.15
f (bar⁻¹)

Fig 2

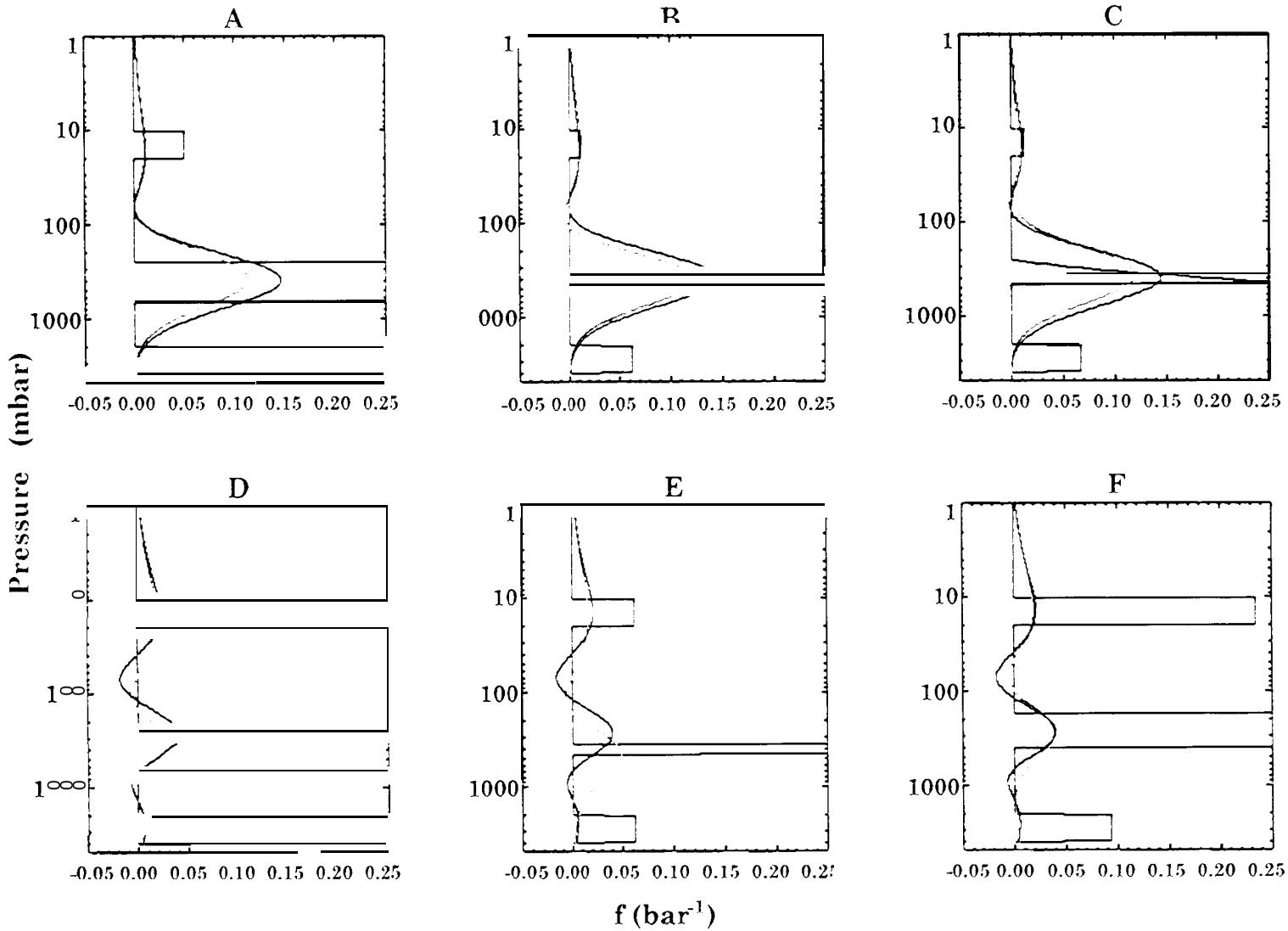
A
B
C
D
E
F
Pressure (mbar)
1
10
100
1000
-0.05 0.00 0.05 0.10 0.15 0.20 0.25
f (bar^{-1})

Fig 3

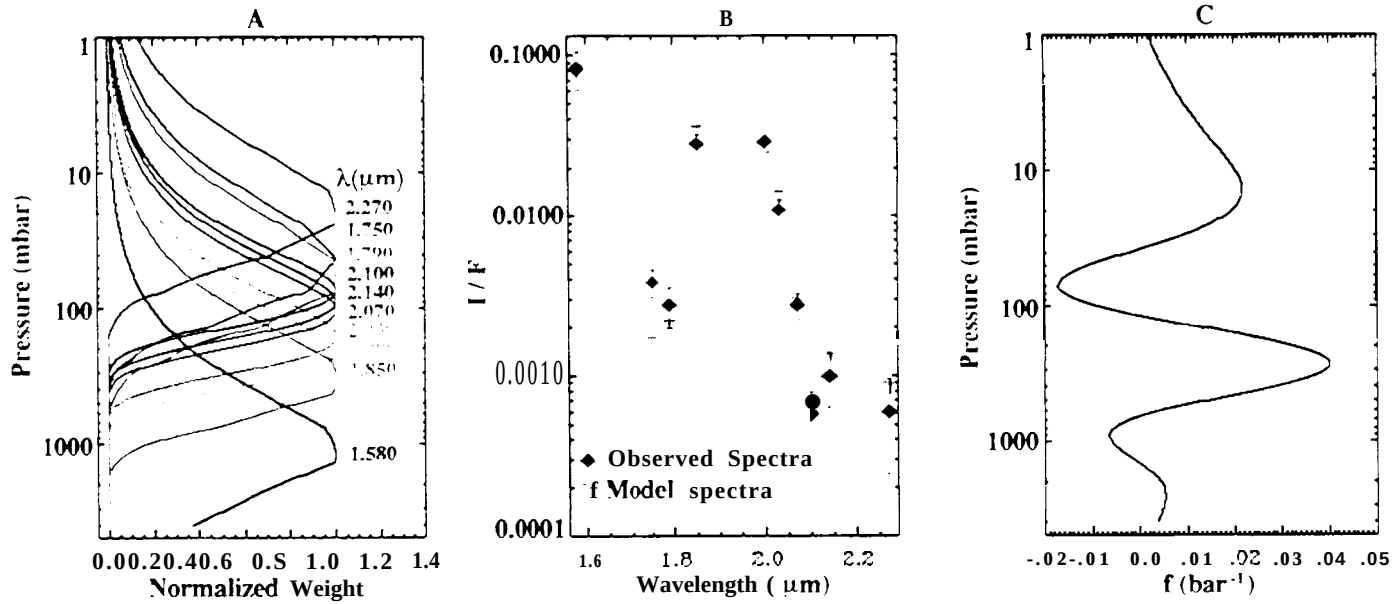
A
B
C
Pressure (mbar)
1
10
100
1000
λ(μm)
2.270
1.750
2.100
2.140
1.580
0.00.20.40.6 0.S 1.0 1.2 1.4
Normalized Weight
I / F
0.1000
0.0100
0.0010
0.0001
◆ Observed Spectra
f Model spectra
1.6 1.8 2.0 2.2
Wavelength (μm)
-.02-.01 0.0 .01 .02 .03 .04 .05
f (bar-1)

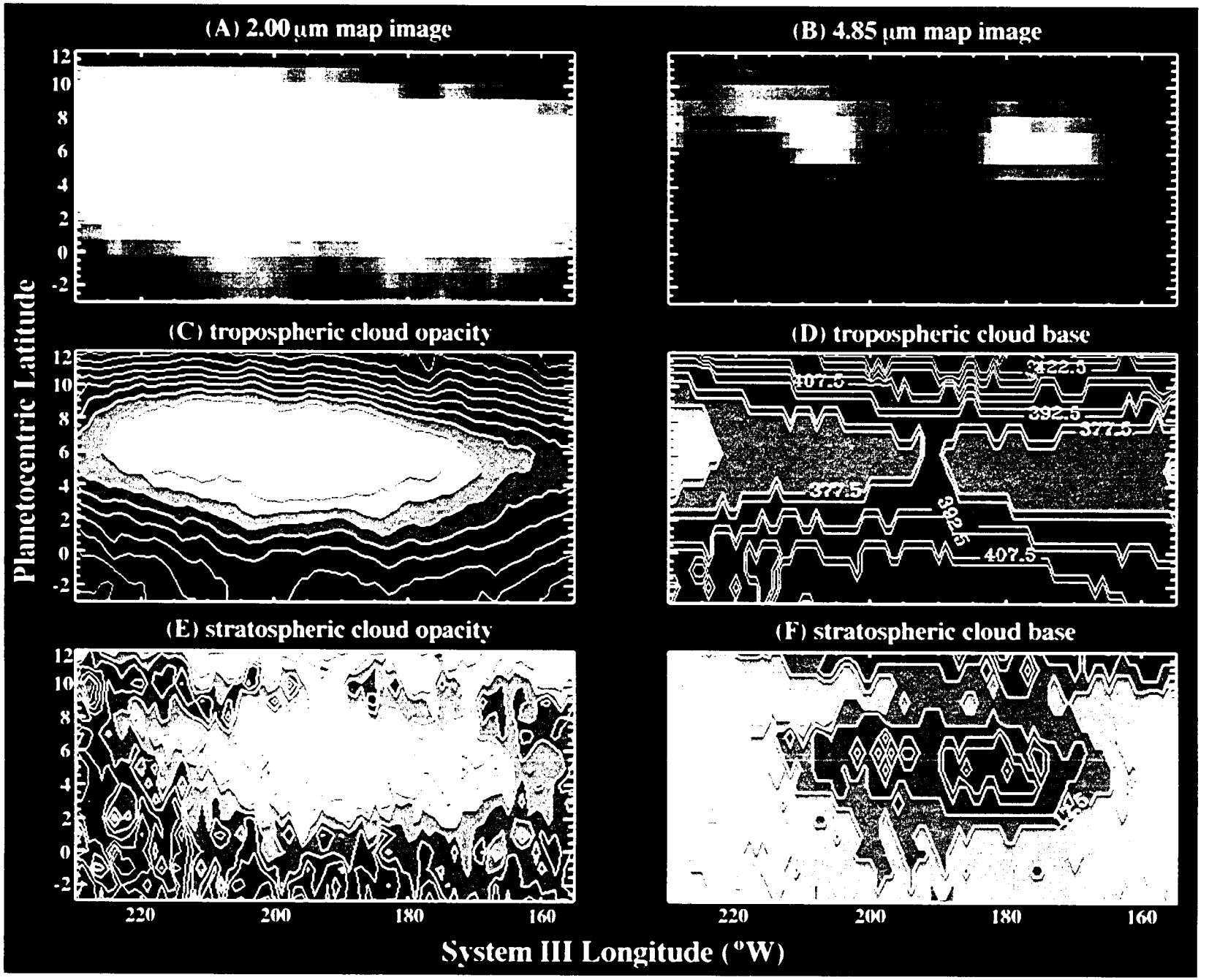
(A) 2.00 μm map image
(B) 4.85 μm map image
(C) tropospheric cloud opacity
(D) tropospheric cloud base
(E) stratospheric cloud opacity
(F) stratospheric cloud base
Planetocentric Latitude
12
10
8
6
4
2
0
-2
407.5
392.5
377.5
220
200
180
160
System III Longitude (°W)

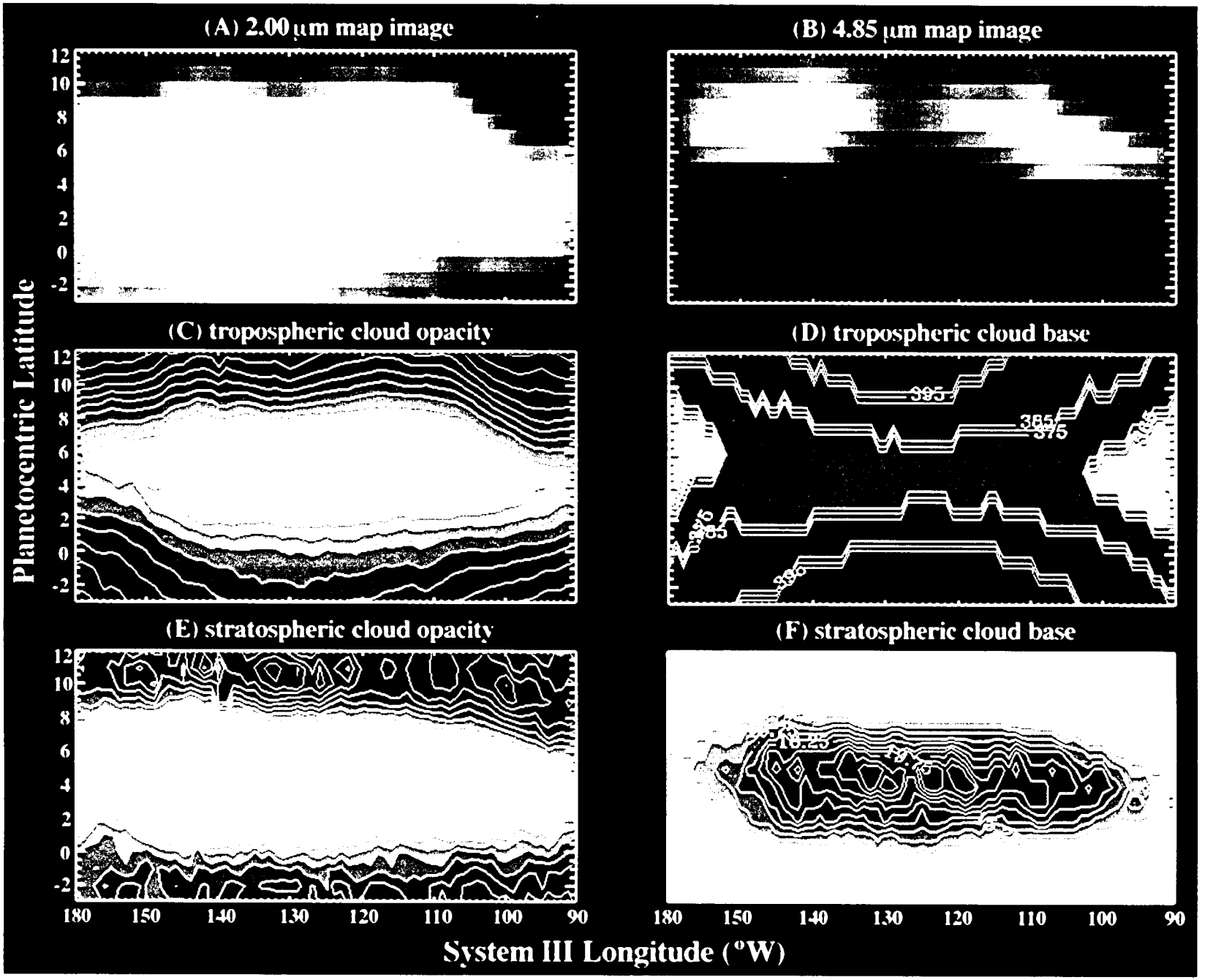
(A) 2.00 μm map image
(B) 4.85 μm map image
(C) tropospheric cloud opacity
(D) tropospheric cloud base
(E) stratospheric cloud opacity
(F) stratospheric cloud base
Planetocentric Latitude
12
10
8
6
4
2
0
-2
395
385
375
365
355
390
16.25
180
150
140
130
120
110
100
90
System III Longitude (°W)

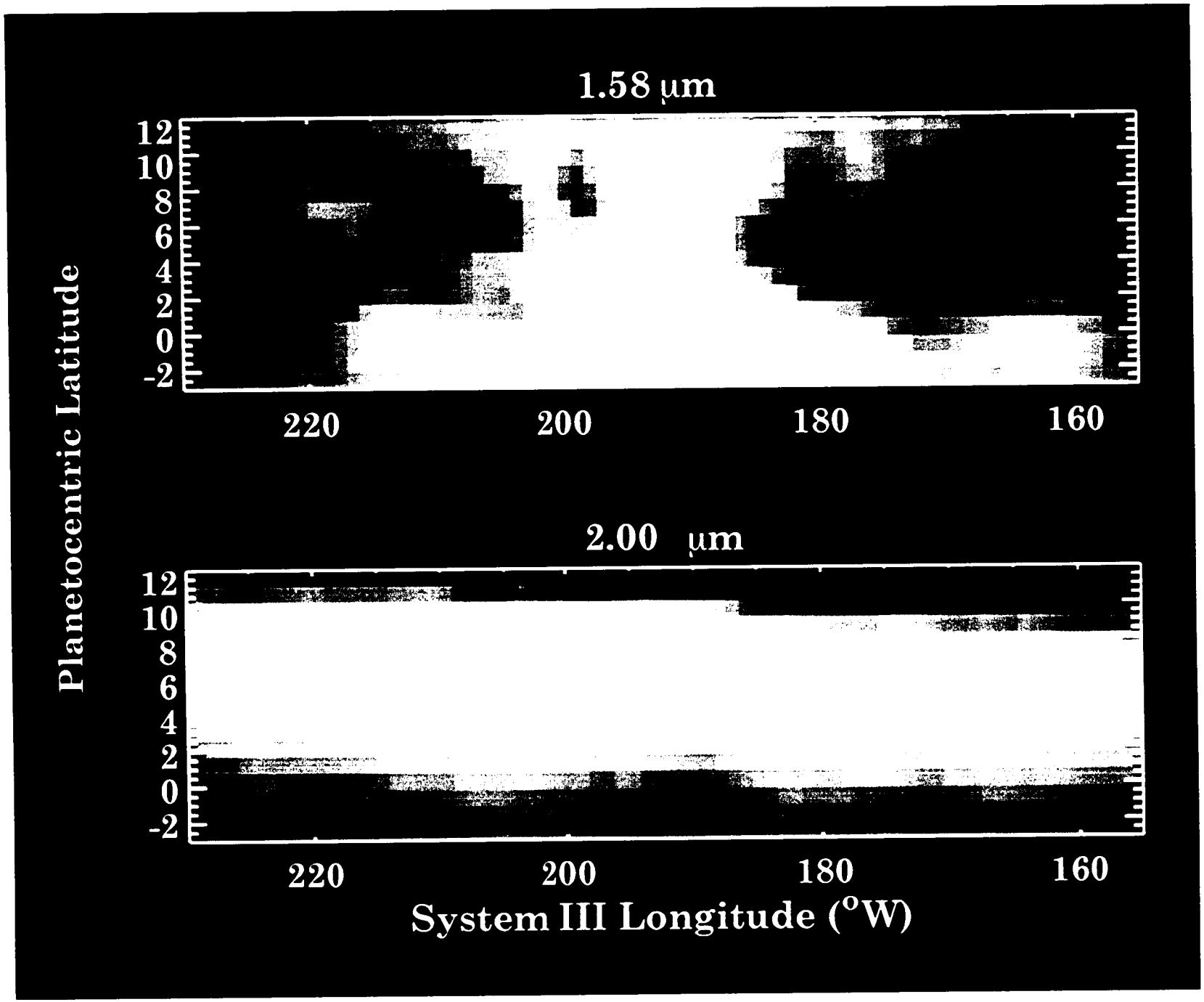
1.58 μm
2.00 μm
Planetocentric Latitude
12
10
8
6
4
2
0
-2
220
200
180
160
System III Longitude (°W)

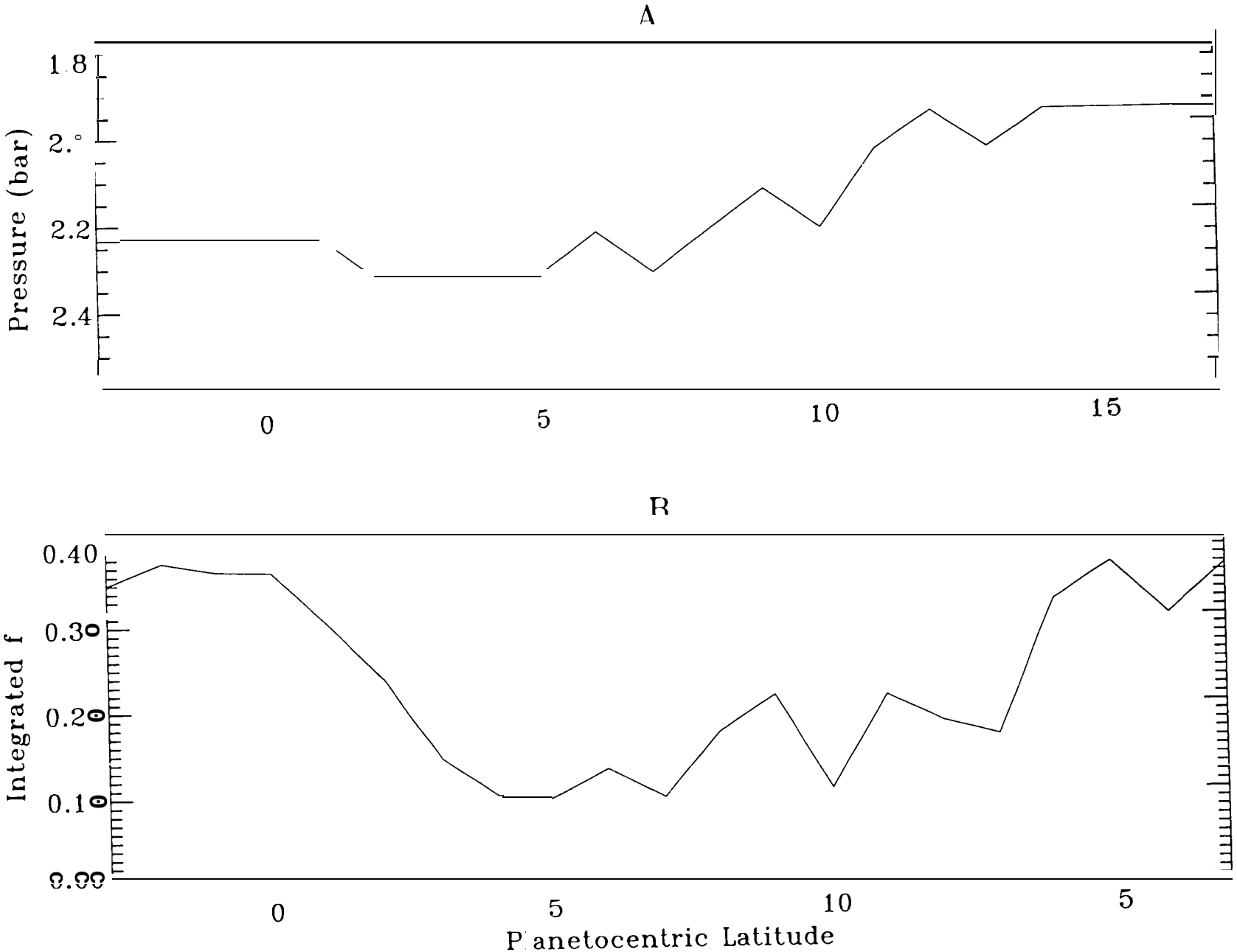
A
1.8
2.0
2.2
2.4
Pressure (bar)
0
5
10
15
B
0.40
0.30
0.20
0.10
0.00
Integrated f
0
5
10
5
Planetocentric Latitude

Fig 8